Investigating Instabilities in the Mammalian Cochlea Using a Stochastic Uncertainty Model

Maurice Filo, *Member, IEEE*, and Bassam Bamieh, *Fellow, IEEE*

***Abstract*—We examine the problem of mean-square stability in a dynamical model of the mammalian cochlea with stochastically uncertain parameters. The cochlea is a mechanical spectrum analyzer with an adaptive gain amplification mechanism that gives it a very large dynamic range as an acoustic sensor. This adaptive gain mechanism has been conjectured to be responsible for occasional instabilities that can be clinically significant. We model the cochlea as a spatio-temporal dynamical system made up of a spatially distributed array of coupled oscillators incorporating an adaptive amplification mechanism. We consider settings where the cochlear amplifier has spatially and temporally varying stochastic parameters. It is shown that relatively small parameter variations (few orders of magnitude smaller than the nominal values) are sufficient to destabilize the dynamics and induce spontaneous oscillations. This extreme sensitivity of the cochlear dynamics appears to be due to a combination of the local cochlear amplification mechanism, as well as the spatial coupling of the distributed resonators. The analysis technique used in this work allows for a simulation-free prediction of the stability thresholds and the statistics of the spontaneous oscillations. Theoretical predictions are verified using full nonlinear stochastic simulations that demonstrate a good agreement with the theoretical predictions.**

***Index Terms*—Cochlear modeling, spontaneous otoacoustic emissions, cochlear amplifier, structured stochastic uncertainty, mean-square stability, feedback systems.**

I. Introduction

THE COCHLEA is a highly sensitive device that is capable of sensing sound waves across a broad spectrum of frequencies (20−20000Hz) and across a wide range of sound intensities ranging from 0dB (threshold of hearing) up to 120dB (sound of a jet engine). The cochlea was believed to be a passive device that acts like a Fourier analyzer: each frequency causes a vibration at a particular location on the basilar membrane (BM). This mechanism was discovered by the Nobel Prize winner Georg von Békésy who carried out his experiments on cochleae of human cadavers. However, in 1948, Thomas Gold hypothesized that the ear is instead an active device that has a component now called the cochlear amplifier. Although Gold's hypothesis was rejected by von Békésy, David Kemp validated it thirty years later by measuring faint sound emissions from the ear. These emissions, termed otoacoustic emissions (OAEs) are sound waves that are produced by the cochlea and can be measured in the ear canal.

It is widely accepted that the outer hair cells, anchored on the cochlear partition, are responsible for the active gain in the cochlea that produces these emissions. However, the underlying mechanism is still not well understood. For example, spontaneous otoacoustic emissions (SOAEs) – emissions generated in the absence of any stimulus – are studied in [1] and [2]. The remarkable high sensitivity of the cochlea makes it vulnerable to stochastic perturbations that are believed to be the cause of these emissions. Particularly, in [2], the authors studied the instabilities that arise in a linear biomechanical cochlear model with spatially random active gain profiles that are static in time. In [1], similar analysis was carried out on simplified cochlear models comprised of coupled active nonlinear oscillators. The randomness, or disorder, was introduced via static variations of a bifurcation parameter. In these previous works, the analysis was carried out through Monte Carlo simulations by studying the stability of different randomly generated active gain (or bifurcation) profiles.

In this paper, we carry out a *simulation-free* stability analysis of the linearized dynamics of a nonlinear model of the cochlea. Our analysis employs structured stochastic uncertainty theory [3], [4], [5] rather than Monte Carlo simulations, where the active gain is stochastic in space and time and may have a spatially-varying expectation and/or covariance. It turns out that letting the active gain be a stochastic process puts the model in a standard setting of linear time-invariant (LTI) systems in feedback with a diagonal stochastic process that enters the dynamics multiplicatively (see Figure 2). This analysis allows us to predict the locations on the BM where the dynamics are more likely to destabilize due to the underlying uncertainties. It also provides a bound on the variance of the perturbations allowed such that stability is maintained.

A brief version of this work [6] appeared in the proceedings of the 57th IEEE Conference on Decision and Control. The current paper includes all the concepts covered in the conference version, but with more mathematical details for the derivations and finite approximations of the linear operators. We also consider an additional scenario where the covariance of the stochastic uncertainties is not constant in space. Furthermore, we carry out a stochastic simulation of the full

Manuscript received January 8, 2020; revised April 30, 2020; accepted May 2, 2020. Date of publication May 11, 2020; date of current version July 15, 2020. This work was supported in part by NSF under Award ECCS-1932777 and Award CMI-1763064. The associate editor coordinating the review of this article and approving it for publication was J. W. Choi. *(Corresponding author: Maurice Filo.)*

Maurice Filo is with the Department of Biosystems Science and Engineering, ETH Zürich, 4058 Zürich, Switzerland (e-mail: maurice.filo@bsse.ethz.ch).

Bassam Bamieh is with the Department of Mechanical Engineering, University of California at Santa Barbara, Santa Barbara, CA 93106 USA (e-mail: bamieh@ucsb.edu).

Digital Object Identifier 10.1109/TMBMC.2020.2993764

nonlinear model of the cochlea to compare it with the predicted theoretical analysis.

The rest of the paper is organized as follows: we start by providing a brief description of a class of biomechanical models of the cochlea in Section II-A. Then, in Section II-B, we recast this class of models in a descriptor state space (DSS) form using operator language (i.e., in continuous space-time). In Section III, we reformulate the DSS form in a standard setting that is particularly useful to carry out our stochastic uncertainty analysis. We also provide the conditions for mean-square stability (MSS). In Section IV, we present the numerical results of the possible instabilities caused by stochastic gain profiles with different statistic properties. To validate our analysis, we show a stochastic simulation for the full nonlinear model in Section V. Finally, before we conclude, we give a discussion in Section VI to give a physical interpretation of our results and provide some comments on previous works.

II. Bio-Mechanical Model of the Cochlea

Throughout the literature, cochlear modeling attempts varied depending on two main factors. The first is concerned with the degree of biological realism of the mathematical model. This is realized by the incorporation of various biological structures [7], [8], [9] and the dimensionality of the fluid filling the cochlear chambers [10], [11]. The second factor is concerned with the computational aspect of the models. Different numerical methods were devised to approach the spatio-temporal nature of the cochlea [12], [13]. Particularly, [14] used a finite difference method developed in [12] to discretize space and formulate the model in state space form. Moreover, computationally efficient methods and model reduction techniques were developed for fast simulations of cochlear response [15], [16]. This section starts by describing the mathematical model adopted in this paper. Then, we reformulate the latter in a continuous space-time descriptor state space form, using operator language. This form has two advantages: (a) it encompasses a wider class of cochlear models and (b) it makes the dynamics more transparent by treating the exact model and its finite dimensional approximation (i.e., discretizing space by some numerical method) separately [17].

A. Mathematical Model Description

The mathematical model can be divided into two main blocks as illustrated in Figure 1(a). For a detailed derivation of the governing mechanics, refer for example to [14] and [16] for a one and two dimensional modeling of the fluid stage, respectively. The fluid block, commonly referred to as the macro-mechanical stage, is linear and memoryless under the appropriate assumptions and approximations (refer to Appendix-A). This block introduces spatial coupling along the different locations on the BM. Its output is the pressure $p(x,\,t)$ acting on each location of the BM. The governing equation can be written in general, regardless of the dimensionality of the fluid and the numerical method used, as

$$p(x,t) = -\big[\mathcal{M}_f \ddot{u}\big](x,t) - [\mathcal{M}_s \ddot{s}](t), \tag{1}$$

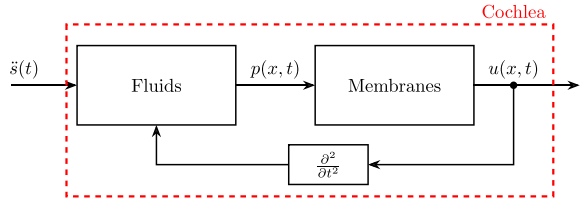

(a) Block Diagram of the Cochlea: The fluids actuate the membranes which, in turn, have a feedback effect on the fluids.

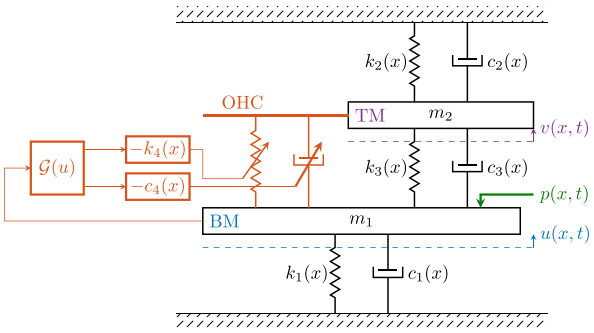

(b) Detailed Schematic Representing the Membranes Block: The BM and TM form a coupled mass-spring-damper system actuated by the fluid pressure at each location x of the BM. The red sub-blocks constitute an adaptive negative damper that provides the model with a source of active energy pumping.

Fig. 1. (a) The cochlea processes the acceleration of the stapes $\ddot{s}(t)$ in two stages, to produce the BM displacement, $u(x,\,t)$, at every location x. The first stage is governed by the fluid that is stimulated by both the stapes and BM accelerations to yield a pressure $p(x,\,t)$ acting on every location of the BM. The second stage is governed by the dynamics of the membranes. The two stages are in feedback through the BM acceleration. (b) This figure is a schematic of a cross section (at a location x) of the cochlear partition showing the membranes governing the dynamics of the micro-mechanical stage. The spatially varying parameters m_i, $c_i(x)$ and $k_i(x)$ are the mass, damping coefficient and stiffness of the BM and TM for $i = 1$ and 2, respectively. Furthermore, $c_3(x)$ and $k_3(x)$ are the mutual damping coefficient and stiffness, respectively; while $c_4(x)$ and $k_4(x)$ are the damping coefficient and stiffness associated with the active feedback gain from the outer hair cells (OHC) to the BM. The spring and damper between the BM and the OHC have variable negative values to capture the effect of the active force acting only on the BM without any direct effect on the TM. Their values depend on the BM displacement u via the nonlinear gain $\mathcal{G}(u)$. Equation(2) describes the underlying dynamics.

where $\ddot{s}(t)$ represents the stapes acceleration, and $\mathcal{M}_f$ and $\mathcal{M}_s$ are linear spatial operators associated with the fluid and stapes mass, respectively. Refer to Appendix-A for a more detailed discussion of these mass operators and their finite dimensional approximations as matrices M_f and M_s, respectively. The second block, commonly referred to as the micro-mechanical stage, takes the distributed pressure $p(x,\,t)$ as an input to produce the BM displacement $u(x,\,t)$ at every location according to the following differential equations

$$\begin{bmatrix} \frac{g}{b}m_1 & 0 \\ 0 & m_2 \end{bmatrix}\begin{bmatrix} \ddot{u} \\ \ddot{v} \end{bmatrix} + \begin{bmatrix} \frac{g}{b}(c_1+c_3-\mathcal{G}(u)c_4) & \mathcal{G}(u)c_4-c_3 \\ -\frac{g}{b}c_3 & c_2+c_3 \end{bmatrix}\begin{bmatrix} \dot{u} \\ \dot{v} \end{bmatrix} + \begin{bmatrix} \frac{g}{b}(k_1+k_3-\mathcal{G}(u)k_4) & \mathcal{G}(u)k_4-k_3 \\ -\frac{g}{b}k_3 & k_2+k_3 \end{bmatrix}\begin{bmatrix} u \\ v \end{bmatrix} = \begin{bmatrix} p \\ 0 \end{bmatrix}, \tag{2}$$

where $v(x,\,t)$ is the tectorial membrane (TM) displacement (refer to Figure 1(b)). Note that the space and time variables $(x,\,t)$ are dropped where necessary for notational compactness.

The constant b is the ratio of the average to maximum vibration along the width of the BM, and g is the BM to outer hair cells lever gain. Refer to [9] for a detailed explanation of the parameters. Finally, $\mathcal{G}$ is the nonlinear active gain operator that captures the active nature of the outer hair cells, commonly referred to as the cochlear amplifier. In the spirit of [8], the action of $\mathcal{G}$ on a distributed BM displacement profile u is given by

$$[\mathcal{G}(u)](x,t) = \frac{\gamma(x)}{1+\theta\Big[\Phi_\eta\Big(\frac{u^2}{R^2}\Big)\Big](x,t)}, \tag{3}$$

where the gain coefficient $\gamma(x)$ represents the gain at a location x, in the absence of any stimulus ($u(x,\,t)=0$). The constants $\theta = 0.5$ and $R = 1$nm are the nonlinear coupling coefficient and BM displacement normalization factor, respectively. The operator Φ_η is a smoothing normalized Gaussian operator such that its action on u is defined as

$$\big[\Phi_\eta(u)\big](x,t) \coloneqq \frac{\int_0^L \phi_\eta(x-\xi)u(\xi,t)d\xi}{\int_0^L \phi_\eta(x-\xi)d\xi}; \tag{4}$$

$$\phi_\eta(x) \coloneqq \frac{1}{\eta\sqrt{2\pi}}e^{\frac{-x^2}{2\eta^2}}, \tag{5}$$

where L is the length of the BM and ϕ_η is the Gaussian kernel with a width η. Note that $\eta = 0.5345$mm corresponds to the Equivalent Rectangular Bandwidth (ERB) on the BM (refer to Appendix-D for a detailed explanation). Observe that the spatial coupling in the micro-mechanical stage appears only in the nonlinear active gain (3) via Φ_η which incorporates the effect of the ERB. Note that other forms of longitudinal coupling exist in the literature, see [18] for example.

Finally, we note that the cochlear amplifier (depicted in red in Figure 1(b)) is mathematically modeled here as a distributed, nonlinear, negative damper. This hides the physiological details of the stereocilia which is not explicitly represented in the mathematical model.

B. Deterministic Descriptor State Space Formulation of the Linearized Dynamics in Continuous Space-Time

This section gives a Descriptor State Space (DSS) formulation of the cochlear model described in (1) and (2). The DSS form is given for the linearized dynamics around the only fixed point which is the origin.

It can be shown (Appendix-C) that the linearized dynamics can be achieved by simply replacing the nonlinear active gain $[\mathcal{G}(u)](x,t)$ in (2) by its gain coefficient $\gamma(x)$. First, define the state space variable $\psi(x,\,t)$ in continuous space-time as

$$\psi(x,t) \coloneqq \begin{bmatrix} u(x,t) & v(x,t) & \dot{u}(x,t) & \dot{v}(x,t)\end{bmatrix}^T. \tag{6}$$

Then the DSS form of the linearized dynamics is

$$\begin{aligned}\mathcal{E}\frac{\partial}{\partial t}\psi(x,t) &= \mathcal{A}_\gamma\psi(x,t) + \mathcal{B}\ddot{s}(t)\\ u(x,t) &= \mathcal{C}\psi(x,t),\end{aligned} \tag{7}$$

where $\mathcal{E}$, $\mathcal{A}_\gamma$ and $\mathcal{B}$ are matrices of linear spatial operators defined as follows

$$\mathcal{E} \coloneqq \begin{bmatrix}\mathcal{I} & 0 & 0 & 0\\ 0 & \mathcal{I} & 0 & 0\\ 0 & 0 & \frac{g}{b}m_1\mathcal{I}+\mathcal{M}_f & 0\\ 0 & 0 & 0 & m_2\mathcal{I}\end{bmatrix};\quad \mathcal{B} \coloneqq \begin{bmatrix}0\\0\\-\mathcal{M}_s\\0\end{bmatrix};$$

$$\mathcal{A}_\gamma \coloneqq \mathcal{A}_0 + \mathcal{B}_0\gamma\mathcal{C}_0;\qquad \mathcal{C} \coloneqq \begin{bmatrix}\mathcal{I} & 0 & 0 & 0\end{bmatrix};$$

$$\mathcal{A}_0 \coloneqq \begin{bmatrix}0 & 0 & \mathcal{I} & 0\\ 0 & 0 & 0 & \mathcal{I}\\ -\frac{g}{b}(k_1+k_3) & k_3 & -\frac{g}{b}(c_1+c_3) & c_3\\ \frac{g}{b}k_3 & -(k_2+k_3) & \frac{g}{b}c_3 & -(c_2+c_3)\end{bmatrix};$$

$$\mathcal{B}_0 \coloneqq \begin{bmatrix}0 & 0 & \mathcal{I} & 0\end{bmatrix}^T;\qquad \mathcal{C}_0 \coloneqq \begin{bmatrix}\frac{g}{b}k_4 & -k_4 & \frac{g}{b}c_4 & -c_4\end{bmatrix};$$

and $\mathcal{I}$ is the identity operator. The equations in (7) represent a deterministic evolution differential equation and an output equation that provides the distributed displacement of the BM $u(x,\,t)$. Other outputs can be selected, such as the TM displacement, by appropriately constructing the $\mathcal{C}$ operator. In the subsequent section, we slightly modify the dynamical equations to account for stochastic perturbations in the gain coefficient $\gamma(x)$.

III. Stochastic Uncertainties in the Active Gain

This section investigates the Mean Square Stability (MSS, which we will formally define in Section III-A) of the linearized cochlear dynamics when the gain coefficient is a *spatio-temporal stochastic process*. The stochastic gain coefficient, now denoted by $\gamma(x,\,t)$ to account for spatio-temporal perturbations, enters the dynamics (7) multiplicatively. We first reformulate the dynamics as an LTI system in feedback with a diagonal stochastic gain which is a standard setting in robust control theory [19, Sec. 10.3]. Then we carry out our MSS analysis based on [4]. By tracking the evolution of the instantaneous spatial covariances, MSS analysis allows us to predict the locations on the BM that are more likely to become unstable due to the underlying stochastic uncertainty. We conclude this section by defining and analyzing a linear operator, whose spectral radius provides a condition for MSS.

A. Stochastic Feedback Interconnection

The purpose of this section is to separate the stochastic portion of the gain coefficient in a feedback interconnection. We assume that $\gamma(x,\,t)$ is a *spatio-temporal stochastic process* that is white in time (but may be colored in space), and whose expectation and covariance are independent of time. More precisely, let $\bar{\gamma}(x)$ be the expectation of $\gamma(x,\,t)$ and $\tilde{\gamma}(x,t)$ be a temporally independent, zero mean stochastic perturbation, such that

$$\begin{aligned}&\gamma(x,t) = \bar{\gamma}(x) + \epsilon\tilde{\gamma}(x,t),\\ &\qquad\text{with}\ \begin{cases}\mathbb{E}[\gamma(x,t)] = \bar{\gamma}(x)\\ \mathbb{E}[\tilde{\gamma}(x,t)\tilde{\gamma}(\xi,\tau)] = \mathbf{\Gamma}(x,\xi)\delta(t-\tau)\end{cases}\quad \forall t\geq 0,\end{aligned} \tag{8}$$

where $\mathbb{E}[.]$ denotes the expectation, ϵ is a perturbation parameter, $\delta(t)$ is the Dirac Delta function, and $\mathbf{\Gamma}(x,\xi)$ is a positive

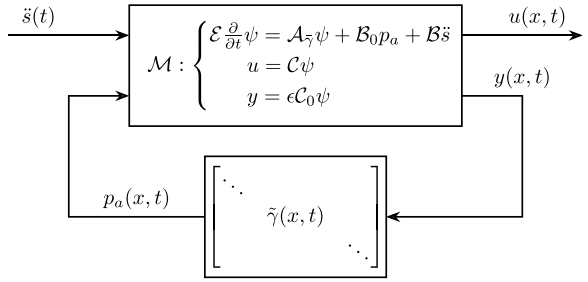

Fig. 2. The linearized cochlear model in feedback with multiplicative stochastic gain. The block to the top represents the deterministic portion of the linearized cochlear dynamics casted in a descriptor state space form. The feedback block is a diagonal spatial operator that represents the multiplicative stochastic gain. *y(x, t)* is the differential displacement and velocity between the BM and TM as given by (10). $p_a(x,t)$ is the active pressure that results from the stochastic component of the active gain.

semi-definite covariance kernel. Substituting (8) in (7) yields

$$\begin{aligned}\mathcal{E}\frac{\partial}{\partial t}\psi(x,t) &= \big(\mathcal{A}_{\bar{\gamma}} + \epsilon\mathcal{B}_0\tilde{\gamma}\mathcal{C}_0\big)\psi(x,t) + \mathcal{B}\ddot{s}(t)\\ u(x,t) &= \mathcal{C}\psi(x,t).\end{aligned} \tag{9}$$

The evolution equation in (9) is a Stochastic Partial Differential Equation (SPDE) that is given an Itō interpretation in the time variable. For more details on Itō calculus, refer to [20].

Define a secondary output related to the difference in BM and TM displacements and velocities as

$$y(x,t) \coloneqq \epsilon\mathcal{C}_0\psi(x,t). \tag{10}$$

Furthermore, define the active feedback pressure resulting from the stochastic perturbations to be

$$p_a(x,t) \coloneqq \tilde{\gamma}(x,t)y(x,t). \tag{11}$$

Therefore, using (9), (10) and (11), construct the feedback block diagram depicted in Figure 2. This is a standard setting [3], [4] for structured stochastic uncertainty analysis, where the feedback gain is a diagonal spatial operator. This configuration is used to investigate the MSS of the cochlea which is formally defined next.

Definition: The feedback system in Figure 2 is MSS if, in the absence of an input (i.e., $\ddot{s}(t) = 0$), the state $\psi(x,t)$ and the active feedback pressure $p_a(x,t)$ have bounded variances for all time.

Therefore, to study MSS, we need to track the temporal evolution of the variances and look at their steady state limits as *t* goes to $+\infty$. This is the topic of the next subsection.

B. Temporal Evolution of the Covariance Operators

This section tracks the time evolution of the covariance operators in the absence of any input (i.e., we set $\ddot{s}(t) = 0$ for the rest of the paper). We use the term covariance "operators" rather than covariance matrices because the spatial variables *x* and ξ are continuous. After using some numerical method to discretize space, the covariance operators can be approximated by covariance matrices. With slight abuse of notation, we use the same symbol to denote the covariance operator and its associated kernel. Define the following instantaneous spatial covariance kernels

$$\begin{aligned}\mathcal{X}(x,\xi;t) &\coloneqq \mathbb{E}[\psi(x,t)\psi(\xi,t)]\\ \mathcal{Y}(x,\xi;t) &\coloneqq \mathbb{E}[y(x,t)y(\xi,t)]\\ \mathcal{P}(x,\xi;t) &\coloneqq \mathbb{E}[p_a(x,t)p_a(\xi,t)]\\ \mathcal{U}(x,\xi;t) &\coloneqq \mathbb{E}[u(x,t)u(\xi,t)]\\ \mathbf{\Gamma}(x,\xi) &\coloneqq \mathbb{E}[\tilde{\gamma}(x,t)\tilde{\gamma}(\xi,t)] \qquad \forall t \geq 0.\end{aligned} \tag{12}$$

Given that the stochastic perturbations $\tilde{\gamma}$ are temporally independent, it can be shown [4, Sec. 5] that the time evolution of the covariance operators are governed by the following operator-valued, *differential algebraic* equations

$$\begin{aligned}\mathcal{E}\dot{\mathcal{X}}\mathcal{E}^* &= \mathcal{A}_{\bar{\gamma}}\mathcal{X}\mathcal{E}^* + \mathcal{E}\mathcal{X}\mathcal{A}_{\bar{\gamma}}^* + \mathcal{B}_0\mathcal{P}\mathcal{B}_0^*\\ \mathcal{Y} &= \epsilon^2\mathcal{C}_0\mathcal{X}\mathcal{C}_0^*\\ \mathcal{P} &= \mathbf{\Gamma}\circ\mathcal{Y},\end{aligned} \tag{13}$$

where $*$ is the adjoint operation and $\circ$ is the Hadamard product; i.e., the element-by-element multiplication of the kernels $\mathcal{P}(x,\xi;t) = \mathbf{\Gamma}(x,\xi)\mathcal{Y}(x,\xi;t)$.

In order to study the MSS, we need to look at the steady state limit of the covariances. We denote by the asymptotic limit of a covariance operator, when it exists, by an overbar. That is

$$\bar{\mathcal{X}} \coloneqq \lim_{t\to\infty}\mathcal{X}(t); \quad \bar{\mathcal{Y}} \coloneqq \lim_{t\to\infty}\mathcal{Y}(t); \quad \bar{\mathcal{P}} \coloneqq \lim_{t\to\infty}\mathcal{P}(t). \tag{14}$$

At the steady state, the covariances become constant in time and thus their time derivatives go to zero. Hence, the steady state covariances, if they exist, are governed by the following operator-valued *algebraic* equations:

$$\begin{aligned}&\mathcal{A}_{\bar{\gamma}}\bar{\mathcal{X}}\mathcal{E}^* + \mathcal{E}\bar{\mathcal{X}}\mathcal{A}_{\bar{\gamma}}^* + \mathcal{B}_0\bar{\mathcal{P}}\mathcal{B}_0^* = 0\\ &\bar{\mathcal{Y}} = \epsilon^2\mathcal{C}_0\bar{\mathcal{X}}\mathcal{C}_0^*\\ &\bar{\mathcal{P}} = \mathbf{\Gamma}\circ\bar{\mathcal{Y}}.\end{aligned} \tag{15}$$

In the next section, we will use (15) to define a new operator as a tool to check the boundedness of the steady state covariances.

C. Loop Gain Operator and MSS

Using (15), define the loop gain operator $\mathbb{L}_{\mathbf{\Gamma}}$, parametrized by the perturbation covariance $\mathbf{\Gamma}$, as

$$\mathbb{L}_{\mathbf{\Gamma}}\big(\bar{\mathcal{P}}_{\text{in}}\big) = \bar{\mathcal{P}}_{\text{out}} \iff \begin{cases}\bar{\mathcal{P}}_{\text{out}} = \mathbf{\Gamma}\circ\big(\mathcal{C}_0\bar{\mathcal{X}}\mathcal{C}_0^*\big)\\ \mathcal{A}_{\bar{\gamma}}\bar{\mathcal{X}}\mathcal{E}^* + \mathcal{E}\bar{\mathcal{X}}\mathcal{A}_{\bar{\gamma}}^* + \mathcal{B}_0\bar{\mathcal{P}}_{\text{in}}\mathcal{B}_0^* = 0.\end{cases} \tag{16}$$

The MSS condition is given in terms of the spectral radius of the loop gain operator as explained next.

Theorem: Consider the system in Figure 2 where $\tilde{\gamma}$ is a temporally independent multiplicative noise, interpreted in the sense of It = o, with instantaneous spatial covariance $\mathbf{\Gamma}$, and $\mathcal{M}$ is a stable causal LTI system. The feedback system is MSS if and only if the spectral radius of the loop gain operator is strictly less than one, i.e.,

$$\epsilon^2\rho(\mathbb{L}_{\mathbf{\Gamma}}) < 1, \tag{17}$$

where $\mathbb{L}_{\mathbf{\Gamma}}$ is defined in (16) and $\rho(\mathbb{L}_{\mathbf{\Gamma}})$ is its spectral radius.

The proof of this theorem is given in [4]. This theorem will be used to find an upper bound on the perturbation constant ϵ above which MSS is violated.

D. Worst-Case Covariances

The loop gain operator maps a covariance operator $\bar{\mathcal{P}}_{\text{in}}$ into another covariance operator $\bar{\mathcal{P}}_{\text{out}}$. Hence, the eigenvectors of $\mathbb{L}_{\mathbf{\Gamma}}$ are themselves operators. When a finite dimensional approximation of $\mathbb{L}_{\mathbf{\Gamma}}$ is carried out using some numerical method, these eigenvectors can be approximated as matrices. We are particularly interested in the eigenvector (or eigen-operator) of $\mathbb{L}_{\mathbf{\Gamma}}$ associated with the largest eigenvalue because it has a significant meaning explained in this subsection.

First, since the loop gain operator is a monotone operator [3], it is guaranteed to have a real largest eigenvalue equal to $\rho(\mathbb{L}_{\mathbf{\Gamma}})$. It is also guaranteed that the eigen-operator associated with the largest eigenvalue is positive semidefinite, i.e., there exists a positive semidefinite covariance operator $\mathbf{P}$ such that

$$\mathbb{L}_{\mathbf{\Gamma}}(\mathbf{P}) = \rho(\mathbb{L}_{\mathbf{\Gamma}})\mathbf{P}. \tag{18}$$

Note that $\mathbf{P}$ is the operator counterpart of the Perron-Frobenius eigenvector for matrices with non-negative entries. Refer to [3, Th. 2.3] for a proof of the aforementioned guarantees. If the stability condition (17) is violated, $\mathbf{P}$ will be the covariance mode that has the highest growth rate, hence the name "worst-case" covariance. This provides information about the locations on the BM that are more likely to destabilize due to the stochastic perturbations of the gain. Particularly, since we are interested in the instabilities at the BM, the worst-case covariance of the BM displacement, denoted by $\mathbf{U}$, can be computed by propagating the worst-case pressure covariance $\mathbf{P}$ through the cochlear dynamics (at steady state) as follows

$$\begin{aligned} &\mathcal{A}_{\bar{\gamma}}\mathbf{X}\mathcal{E}^* + \mathcal{E}\mathbf{X}\mathcal{A}_{\bar{\gamma}}^* + \mathcal{B}_0\mathbf{P}\mathcal{B}_0^* = 0 \\ &\mathbf{U} = \mathcal{C}\mathbf{X}\mathcal{C}^*, \end{aligned} \tag{19}$$

where $\mathbf{X}$ denotes the worst-case covariance operator corresponding to the state space variable ψ.

IV. Instabilities in Linearized Cochlear Dynamics

This section contains the main results on the effects of stochastic uncertainties on cochlear instabilities. The analysis is carried out for three different scenarios of the perturbation covariance $\mathbf{\Gamma}(x,\xi)$:

- $\mathbf{S}_1$*:* spatially uncorrelated uncertainties, i.e., $\mathbf{\Gamma}(x,\xi) = \delta(x-\xi)$
- $\mathbf{S}_2$*:* spatially correlated uncertainties with a correlation length λ, i.e., $\mathbf{\Gamma}(x,\xi) = \phi_\lambda(x-\xi)$
- $\mathbf{S}_3$*:* spatially localized and uncorrelated uncertainties, i.e., $\mathbf{\Gamma}(x,\xi) = \phi_\sigma(x-\mu)\delta(x-\xi)$,

where ϕ_λ and ϕ_σ are the Gaussian kernels defined in (5) such that λ is the spatial correlation length and σ is the spatial localization length centered at $x=\mu$. In the subsequent analysis, scenarios $\mathbf{S}_1$ and $\mathbf{S}_2$ are treated simultaneously because, in both cases, the perturbation covariance is a Toeplitz operator since $\mathbf{\Gamma}(x,\xi)$ depends solely on the difference $x-\xi$ rather than the absolute locations x and ξ. However, in scenario $\mathbf{S}_3$, the perturbation covariance is spatially localized and $\mathbf{\Gamma}(x,\xi)$ depends on the absolute locations, and thus it is treated separately in Section IV-D. Note that this scenario treats situations where stochastic disturbances enter locally in particular regions of the BM (e.g., nearby neural firings), and not globally across its length. Recall that the linearized cochlear dynamics excludes micro-mechanical spatial coupling along different locations of the BM; whereas, scenario $\mathbf{S}_2$ sort of reintroduces spatial coupling via the spatial correlations of the stochastic active gain.

The condition of MSS (17) can be rewritten as

$$\epsilon < \frac{1}{\sqrt{\rho(\mathbb{L}_{\mathbf{\Gamma}})}}, \tag{20}$$

for scenarios $\mathbf{S}_1, \mathbf{S}_2$ and $\mathbf{S}_3$. This bound is the maximum allowed perturbation in (9) such that MSS is maintained. In this section, we compute the upper bound on ϵ and the "worst-case" covariance $\mathbf{U}$ for the linearized cochlear dynamics.

A. Numerical Considerations

This section describes the numerical considerations of the model and the numerical method used to compute the spectral radius and worst-case covariance of $\mathbb{L}_{\mathbf{\Gamma}}$.

The numerical values of the parameters in this paper are taken from Table I in [2] for the linear cochlea. However, the expectation of the gain coefficient, $\bar{\gamma}(x)$, (which was considered to be spatially constant in [2]) is left as a spatially distributed parameter to be tuned. The fluids block in Figure 1(a) considered here is the one dimensional traveling wave as described in Appendix-A. A spatial discretization grid of step size $\Delta_x := L/N_x$, where $N_x = 400$, is used to give a finite dimensional approximation of the operators (as matrices) describing the dynamics in Figure 2 (refer to Appendix-B). Note that the discretization step Δ_x was chosen to be small enough to guarantee a high accuracy for the numerical calculations (see [17] for more details).

Special care has to be taken when dealing with spatially white continuous processes (Scenario $\mathbf{S}_1$). Let Γ denote a matrix approximation of the uncertainty covariance operator $\mathbf{\Gamma}$ and approximate the Dirac delta function as

$$\begin{aligned} \delta(x) \quad &\approx \quad \frac{1}{\Delta_x}\,\text{rect}_{\Delta_x}(x) \\ \text{where} \quad \text{rect}_{\Delta_x} &:= \begin{cases} 1, & \text{if } -\frac{\Delta_x}{2} \le x \le \frac{\Delta_x}{2} \\ 0, & \text{otherwise} \end{cases}. \end{aligned} \tag{21}$$

Hence, the finite dimensional approximation of the perturbation covariance needs to be scaled with the discretization step Δ_x as follows

$$\Gamma = \frac{1}{\Delta_x} I, \tag{22}$$

where I is the identity matrix.

Furthermore, our analysis requires the computation of the largest eigenvalue of the loop gain operator and its associated eigenvector (or eigen-operator). The matrices that approximate the spatial operators have a size of $(4(N_x+1) = 1604)$, and

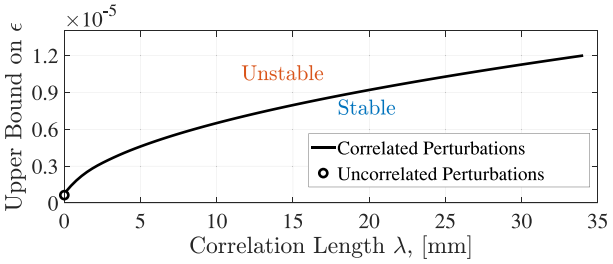

Fig. 3. Mean Square Stability Curve: Upper bound on the perturbation parameter, ϵ, of the stochastic gain (8) whose expectation is $\bar{\gamma}(x) = 1$. The black dot corresponds to scenario $\mathbf{S}_1$ (uncorrelated gain perturbations) and the solid black line corresponds to scenario $\mathbf{S}_2$ (correlated gain perturbations) for different spatial correlation lengths λ. The figure shows that larger correlation lengths make the model more immune to stochastic perturbations.

keeping track of the underlying sparsity of all the approximated operators is essential for carrying out the computations efficiently. Note that to maintain the sparsity of (16) for scenario $\mathbf{S}_2$, we use a truncated Gaussian kernel to approximate ϕ_λ given in (5), i.e., $\phi_\lambda(x-\xi) \approx 0, \text{for}\,|x-\xi| > d$, where d is a pre-specified constant that represents a compromise between computational accuracy and sparsity. Finally, the power iteration method is employed for eigenvalue and eigenmatrix computations as recommended by [21]. This requires solving the Lyapunov-like equation in (16) at each iteration.

B. Stochastic Gain Coefficient With a Spatially Constant Expectation

In this section, we set the expectation of the gain coefficient to one everywhere along the BM, i.e., $\bar{\gamma}(x) = 1$. To study the effects of the spatial correlations in the gain coefficient, we compare scenarios $\mathbf{S}_1$ and $\mathbf{S}_2$ by keeping in mind that $\mathbf{S}_1$ can be seen as a special case of $\mathbf{S}_2$ at the limit when λ goes to zero. First, we compute the upper bounds on ϵ in (20) such that MSS is maintained. Then we compute the worst-case covariance $\mathbf{U}$ in (19).

By applying the power iteration method on (18), we compute the spectral radii $\rho(\mathbb{L}_{\mathbf{\Gamma}})$ and their associated eigen-operators $\mathbf{P}$ for scenarios $\mathbf{S}_1$ and $\mathbf{S}_2$ with different correlation lengths λ. Then, (20) yields the upper bounds on ϵ. The results are illustrated in Figure 3 showing the small upper bounds on ϵ. This reflects the high sensitivity of the model to such stochastic perturbations. As one would expect, a larger correlation length λ requires a larger perturbation to destabilize the linearized cochlea.

The eigen-operator $\mathbf{P}$ computed by the power iteration method is the worst-case pressure covariance. The corresponding worst-case covariance of the BM displacement $\mathbf{U}$ is then computed using (19). Figure 4(a) shows $\mathbf{U}$ for scenario $\mathbf{S}_1$, zoomed in for $0 \le x, \xi \le L/10$. The intensity plot shows two sets of axes. The first axis represents the location on the BM and the second represents the corresponding characteristic frequency at each location, calculated using the Greenwood [22] location-to-frequency mapping.[1] Observe that

[1]Every location on the BM responds maximally to a particular sound frequency, termed the characteristic frequency. Sounds with high (resp. low) frequencies cause vibration near the stapes at $x = 0$ (resp. apex at $x = L$).

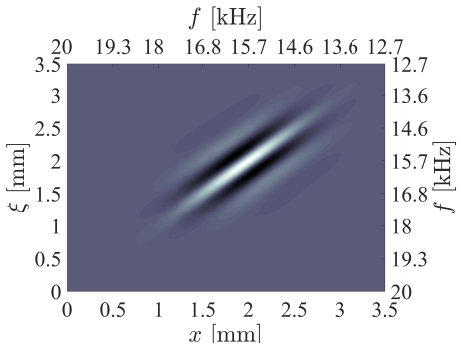

(a) Worst-Case Covariance $\mathbf{U}(x,\xi)$ of the BM Displacement: The covariance that has the fastest growth rate when the dynamics are unstable. Note that the axes are zoomed in $(0 \le x, \xi \le L/10)$ to emphasize the covariance dominance near the stapes.

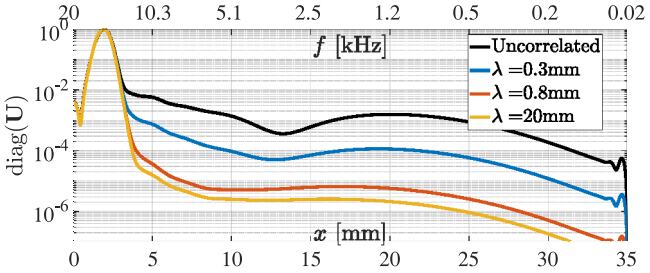

(b) Diagonal Entries of $\mathbf{U}$: The diagonal components are negligible far from the stapes.

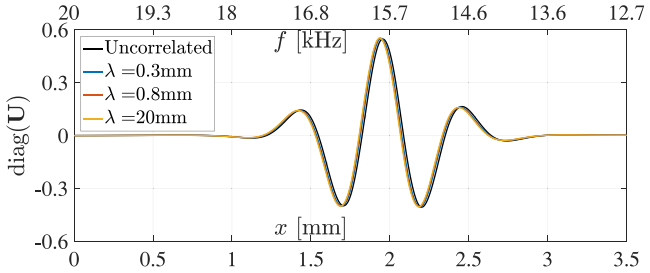

(c) Dominant Eigenfunction of $\mathbf{U}$ (zoomed in): This mode is the most energetic component in the spontaneous BM vibrations caused by the instability.

Fig. 4. Figure (a) shows an intensity plot of the worst-case covariance $\mathbf{U}$ for scenario $\mathbf{S}_1$ (uncorrelated gain perturbation) zoomed in for $0 \le x, \xi \le 3.5$mm. The axes correspond to the physical location x in mm on the BM and the corresponding characteristic frequency f in kHz. Furthermore, the gray shades range between black (for minimum negative values) and white (for maximum positive values). Figure (b) shows the diagonal entries of $\mathbf{U}$ for scenarios $\mathbf{S}_1$ and $\mathbf{S}_2$ for different correlation lengths λ. Figure (c) depicts the dominant eigenfunction of $\mathbf{U}$ for the different cases. Figure (c) indicates the insignificant effect of λ on the shape of the dominant eigenfunctions.

the covariance is band limited and the diagonal entries are dominant near the stapes (x<3 *mm*). This shows that instabilities essentially occur at high frequencies. Figure 4(b) plots the diagonal entries of $\mathbf{U}$ for scenarios $\mathbf{S}_1$ and $\mathbf{S}_2$ for different correlation lengths λ. A smaller correlation length gives a slightly broader spectrum of unstable frequencies. However, for small ϵ, the effect of the correlation length on the shape of the unstable BM modes is negligible. This is illustrated in Figure 4(c), where the dominant eigenfunction of $\mathbf{U}$ is plotted for different cases.

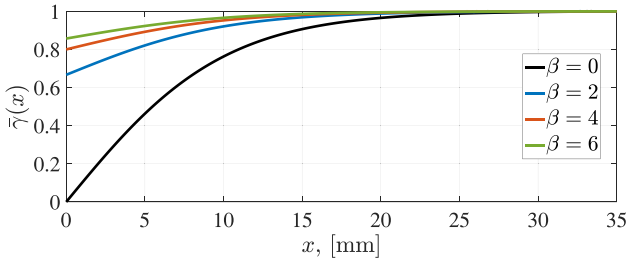

(a) Gain Coefficient Expectation Profiles: Four mean gain profiles with different gain levels near the stapes.

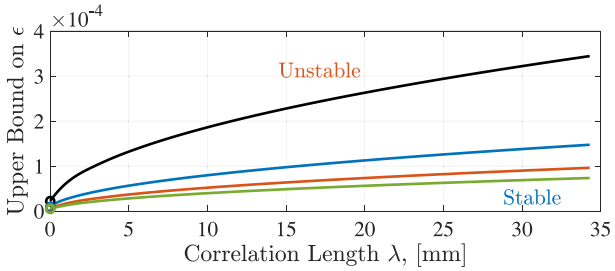

(b) Corresponding MSS Curves: Smaller gain coefficients near the stapes have larger margins of stability.

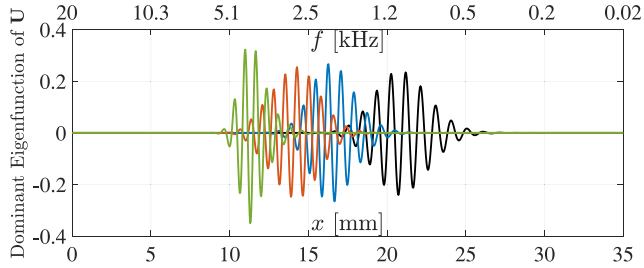

(c) Eigenfunctions for scenario $\mathbf{S}_1$: The dominant vibration modes shift towards the apex when lower gain levels are applied near the stapes.

Fig. 5. Mean Square Stability Curves for different gain coefficient expectation profiles: Figure(a) shows four different profiles of $\bar{\gamma}(x)$ generated as examples of spatially varying gain coefficients using (23). The same values of β are used in figures (b) and (c). Particularly, Figure(b) shows the upper bound on the perturbation parameter ϵ for the corresponding profiles of $\bar{\gamma}(x)$ in Figure(a). The circles correspond to scenario $\mathbf{S}_1$ (uncorrelated gain perturbations) and the solid lines correspond to scenario $\mathbf{S}_2$ (correlated gain perturbations) for different spatial correlation lengths λ. Figure (c) shows the eigenfunctions of the worst-case covariance operator $\mathbf{U}$ corresponding to the different profiles of $\bar{\gamma}(x)$. The peaks of the eigenfunctions shift consistently with the shape of the gain profiles.

C. Stochastic Gain Coefficient With a Spatially Varying Expectation

This section shows that the frequencies of instabilities (or, equivalently, the locations on the BM) can shift depending on the shape of the expectation of the gain coefficient $\bar{\gamma}(x)$. For illustration purposes, four different profiles of $\bar{\gamma}(x)$ are generated as

$$\bar{\gamma}(x) = \frac{\tanh(x/10) + \beta}{\tanh(L/10) + \beta}, \tag{23}$$

where x and L are expressed in mm and $\beta = 0, 2, 4$ and 6. These profiles are only intended to serve as examples, but other profiles can also be used. First, we show the MSS curves, similar to Figure 3 for the four different profiles generated using (23). Figure 5(b) clearly shows that the shape of $\bar{\gamma}(x)$ affects the margin of MSS. Particularly, the larger the dip in the gain coefficient, the higher ϵ needs to be to destabilize the linearized dynamics in the MSS sense.

Observe that the correlation length for small values of ϵ has a negligible effect on the shape of the unstable modes as shown in Figure 4(c). Hence, in this section we only present the worst-case covariances for scenarios $\mathbf{S}_1$. In fact, the correlation length only affects the margin of stability as illustrated in Figure 5(b). Figure 5(c) depicts the dominant eigenfunctions of $\mathbf{U}$ for the four different profiles of $\bar{\gamma}(x)$. Clearly, the peaks of the unstable modes of the BM shift depending on the shape of $\bar{\gamma}(x)$. In fact, as the dip in $\bar{\gamma}(x)$ is increased, the peaks shift farther from the stapes resulting in instabilities of lower frequencies. Figures 4 and 5 suggest that there is a sort of a "weak spot" near the stapes (high frequencies) that destabilizes due to stochastic perturbations in the gain coefficient. This "weak spot" shifts farther from the stapes when a lower gain is applied around the stapes.

D. Stochastic Gain Coefficient With a Spatially Localized Covariance

We now treat the case where the gain coefficient $\gamma(x,t)$ in (9) has a spatially constant expectation, but spatially localized covariance given in scenario $\mathbf{S}_3$, i.e.,

$$\bar{\gamma}(x) = 1 \qquad \text{and} \qquad \mathbf{\Gamma}(x,\xi) = \phi_\sigma(x-\mu)\delta(x-\xi),$$

for different values of σ and μ. Observe that for this form of $\mathbf{\Gamma}(x,\xi)$, the covariance is localized around μ. Hence, this section investigates the cochlear instabilities that emerge as a result of stochastic perturbations localized around a particular location on the BM.

In particular, we are interested in tracking the unstable BM modes for different values of μ and σ, where μ is the location of the perturbation and σ represents the local spread of the perturbation in the neighborhood of μ. Following the same calculations of the previous sections, we compute the dominant eigenfunction of the worst-case covariance of the BM displacement $\mathbf{U}$ for different values of μ and σ. The results are depicted in Figure 6. Observe that localized perturbations of the active gain coefficient at some location μ of the BM causes instabilities in that neighborhood. Particularly, for relatively small spread $\sigma = L/100$, the instabilities emerge at the same locations of the perturbations as shown in Figure 6(a). However, as the spread of the uncertainty is increased up to $\sigma = L/30$ and $L/10$, the location of the instability shifts towards the stapes. In fact, the wider the spread the larger the shift is as illustrated in Figures 6(b) and (c).

This "basal shifting" resembles the phenomenon of detuning observed in the cochlea. Acting as a frequency analyzer (or "inverse-piano"), each location on the BM vibrates in response to a sound stimulus at a particular frequency. Thus, the BM has a frequency-to-location map such that every stimulus frequency has a preferred place on the BM called Characteristic Place (CP). The detuning phenomenon is observed as the shifting of the CP towards the stapes as the intensity of the stimulus (in dB) is increased. In this section, we showed that increasing the spread of the stochastic perturbations also shifts the BM vibrations towards the stapes.

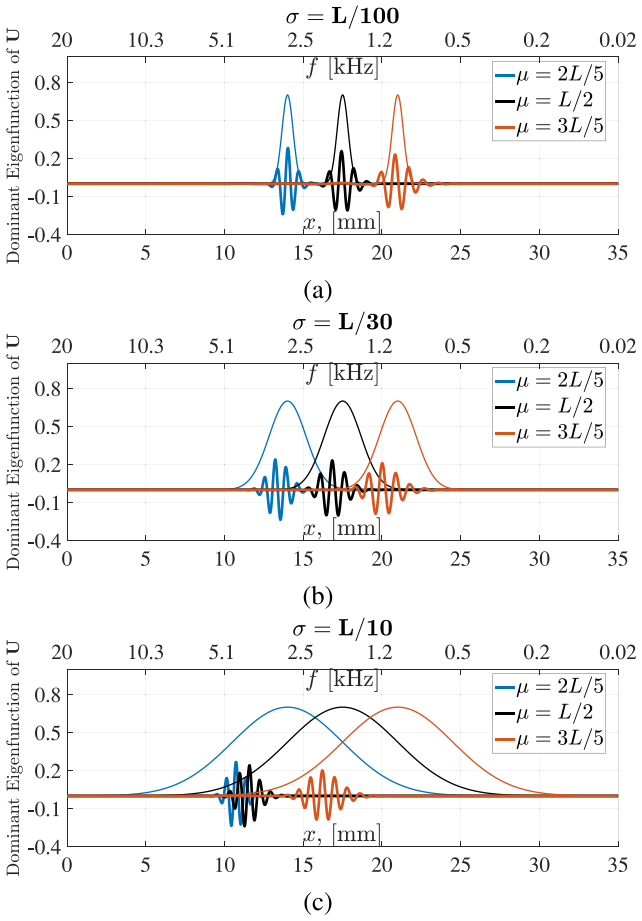

Fig. 6. Eigenfunctions of the worst-case covariance operator $\mathbf{U}$ for different localized gain coefficient perturbations. These figures show the dominant eigenfunctions of the worst-case covariance operators for three different values of μ and σ. Particularly, in each figure, we fix σ and vary μ. Each thin curve represents a particular uncertainty spread function $\phi_\sigma(x-\mu)$ (not drawn to scale in the vertical axis) and each thick curve (with the same color) represents the corresponding dominant eigenfunction of the worst-case covariance operator. This figure illustrates the "basal shifting" observation that resembles the phenomenon of detuning.

Nonlinear dynamics are necessary to model the detuning phenomenon. However, modeling this "detuning-like" phenomenon does not require nonlinearities, instead a locally perturbed active gain is sufficient to explain it.

It is believed that these instabilities in the BM reflect back to the middle ear causing SOAEs [23]. It is also believed that, in a relatively few cases, if these mechanical BM vibrations are intense enough, they can be perceived as tinnitus. In fact, a study in [24] showed that about 4% of cases of tinnitus can be tracked to mechanical origins, and the majority are linked to pure neural origins. Our results suggest a mechanism that explains the frequencies that can be detected in the ear canal due to SOAEs and/or perceived as tinnitus. As a matter of fact, the shape of the statistics (expectation and covariance) of the gain coefficient is a factor that controls the bands of the frequencies that are emitted as SOAEs. These emissions arise due to (a) *spatially variant inhomogeneities* along the cochlear partition and (b) *temporal stochastic perturbations* that give rise to structured stochastic uncertainties.

V. Nonlinear Stochastic Simulations

So far, the MSS analysis is carried out on the linearized dynamics. In this section, we carry out stochastic simulations of the nonlinear model to validate the predictions of our analysis of the linearized dynamics.

A. Nonlinear Descriptor State Space Formulation in Continuous Space-Time

We first start by formulating the nonlinear dynamics in a DSS form similar to that given in Section II-B. Recall that, the nonlinear deterministic active gain is given by (3) with $\gamma(x)$ representing the gain coefficient. To include stochastic perturbations, we substitute (8) in (3) so that the nonlinear stochastic active gain can be written as

$$[\mathcal{G}(u)](x,t) = \frac{\bar{\gamma}(x)+\epsilon\tilde{\gamma}(x,t)}{1+\theta\Big[\Phi_\eta\Big(\frac{u^2}{R^2}\Big)\Big](x,t)} =: (\bar{\gamma}(x)+\epsilon\tilde{\gamma}(x,t))\Big[\tilde{\mathcal{G}}(u)\Big](x,t). \quad (24)$$

Recall that Φ_η is the Gaussian spatial operator given by (4), $\theta = 0.5$, $R = 1$nm and $\eta = 0.5345$mm. By substituting (24) in (2), we can rewrite the nonlinear model in a nonlinear DSS form as

$$\mathcal{E}\frac{\partial}{\partial t}\psi(x,t) = \Big(\mathcal{A}_{\bar{\gamma}}(u) + \epsilon\tilde{\mathcal{B}}_0(u)\tilde{\gamma}\mathcal{C}_0\Big)\psi(x,t), \quad (25)$$

where $\mathcal{A}_{\bar{\gamma}}(u) := \mathcal{A}_0 + \tilde{\mathcal{B}}_0(u)\bar{\gamma}\mathcal{C}_0$ and $\tilde{\mathcal{B}}_0(u)\tilde{\gamma}\mathcal{C}_0$ are nonlinear spatial operators that represent the deterministic and stochastic portions of the dynamics, respectively. Note that $\mathcal{E}, \mathcal{A}_0$, and $\mathcal{C}_0$ are all defined in (7), and $\tilde{\mathcal{B}}_0(u) = \begin{bmatrix}0 & 0 & \tilde{\mathcal{G}}(u) & 0\end{bmatrix}^T$. Therefore, (25) represents the nonlinear stochastic dynamics given in a DSS operator form, where the spatial variable is continuous. This is really a Stochastic Partial Differential Equation (SPDE) that needs to be discretized in space and time in order to carry out our simulations.

B. Description of the Numerical Method for Simulations

In this section, we discretize (25) in space and time so that numerical simulations become fairly straightforward to implement. On a side note, if the stochastic perturbation $\tilde{\gamma} = 0$, (25) becomes a deterministic Partial Differential Equation (PDE). This can be easily integrated by discretizing space using a spatial grid, and then employ a time marching solver such as ODE45 in MATLAB. However, for an SPDE, one has to carefully treat the scaling of the covariances with the discretization steps.

Space and time are discretized as $x_i = i\Delta_x$ and $t_n = n\Delta_t$ with discretization steps $\Delta_x = L/N_x$ and $\Delta_t = t_f/N_t$ for $i = 0, 1, \ldots, N_x$ and $n = 0, 1, \ldots, N_t$, where t_f is the final time. Let the BM and TM displacements on the discretized space-time grid be denoted by the vectors u_n and $v_n \in \mathbb{R}^{N_x+1}$, respectively such that

$$u_n := \begin{bmatrix}u(x_0,t_n) & \cdots & u(x_{N_x},t_n)\end{bmatrix}^T;$$
$$v_n := \begin{bmatrix}v(x_0,t_n) & \cdots & v(x_{N_x},t_n)\end{bmatrix}^T.$$

Then the discretized state space variable can be expressed by $\psi_n \in \mathbb{R}^{4(N_x+1)}$ as

$$\psi_n := \begin{bmatrix} u_n^T & v_n^T & \dot{u}_n^T & \dot{v}_n^T \end{bmatrix}^T.$$

For scenarios $\mathbf{S}_1$ and $\mathbf{S}_3$, $\tilde{\gamma}(x,t)$ is a zero-mean white process in space and time. It can be approximated at the spatial grid points $\{x_i\}_{i=0,1,\dots,N_x}$ and at time t_n as follows

$$\begin{bmatrix} \tilde{\gamma}(x_0,t_n) & \tilde{\gamma}(x_1,t_n) & \cdots & \tilde{\gamma}(x_{N_x},t_n) \end{bmatrix}^T \approx \frac{1}{\sqrt{\Delta_x \Delta_t}} w_n,$$

where $w_n \in \mathbb{R}^{N_x+1}$ is a zero-mean Gaussian random vector with a covariance matrix $\mathbb{E}[w_n w_n^T] = I$ for $\mathbf{S}_1$ and $\mathbb{E}[w_n w_n^T] = \mathcal{D}(\begin{bmatrix} \phi_\sigma(x_0-\mu) & \cdots & \phi_\sigma(x_{N_x}-\mu) \end{bmatrix})$ for $\mathbf{S}_3$, where $\mathcal{D}$ is the diagonal operator such that $\mathcal{D}(w_n)$ is a diagonal matrix with w_n arranged on its diagonal entries.

For scenario $\mathbf{S}_2$, $\tilde{\gamma}(x,t)$ is a stochastic process that is white in time but "colored" in space with a spatial covariance $\mathbf{\Gamma}(x,\xi) = \epsilon^2 \phi_\lambda(x-\xi)$. In this scenario, the noise is smooth in space and there is no need to scale the covariance by the spatial discretization step. More precisely, $\tilde{\gamma}(x,t)$ can be approximated as

$$\begin{bmatrix} \tilde{\gamma}(x_0,t_n) & \tilde{\gamma}(x_1,t_n) & \cdots & \tilde{\gamma}(x_{N_x},t_n) \end{bmatrix}^T \approx \frac{1}{\sqrt{\Delta_t}} w_n,$$

where $\mathbb{E}[w_n w_n^T]$ is now a symmetric matrix whose $(i,j)^{\text{th}}$ entry is given by $\phi_\lambda(x_i - x_j)$.

Therefore, a first order approximation of (25) can be carried out in the spirit of the Euler-Maruyama method [25] to obtain

$$E\psi_{n+1} = E\psi_n + \Delta_t A_{\bar{\gamma}}(u_n)\psi_n + \alpha \tilde{B}_0(u_n)\mathcal{D}(w_n)C_0\psi_n \tag{26}$$

where $\alpha = \epsilon\sqrt{\Delta_t/\Delta_x}$ for $\mathbf{S}_1$ and $\mathbf{S}_3$; and $\alpha = \epsilon\sqrt{\Delta_t}$ for $\mathbf{S}_2$. The matrices $E, A_{\bar{\gamma}}(u_n)$, $\tilde{B}_0(u_n)$ and C_0 are all finite dimensional approximations of the operators $\mathcal{E}, \mathcal{A}_{\bar{\gamma}}(u)$, $\tilde{\mathcal{B}}_0(u)$ and $\mathcal{C}_0$, respectively (see Appendix-B). Equation (26) represents the recursive numerical methods to solve (25) for all three scenarios with the right choice of α and $\mathbb{E}[w_n w_n^T]$.

C. Simulation of the Nonlinear Stochastic Model

To validate our MSS analysis of the linearized dynamics and evaluate how well it copes with the nonlinear dynamics, we carry out a simulation of (25). This section considers scenario $\mathbf{S}_1$. Hence, the numerical method used here is that given in (26) for $\alpha = \epsilon^2\sqrt{\Delta_t/\Delta_x}$ and $\mathbb{E}[w_n w_n^T] = I$.

The nonlinear stochastic simulation shown here is for $\bar{\gamma}(x)$ given in (23) with $\beta = 2$. All other scenarios are in agreement with our MSS analysis; however, this particular case study ($\beta = 2$) is chosen here to illustrate the effectiveness of our analysis. Observe using Figure 5(b) that for $\beta = 2$, the MSS condition is violated if $\epsilon \geq 9.1 \times 10^{-6}$. We choose $\epsilon = 1.1 \times 10^{-5}$ which slightly violates the MSS condition for the linearized dynamics and allows the nonlinearity to kick in and saturate the response. The spatio-temporal response of the BM is depicted in Figure 7(a) for $t \in [0, t_f]$ with $t_f = 200$ms. This response depicts a single stochastic simulation for a particular realization of the stochastic uncertainty. The response is maximal in a band limited region 10mm $< x <$ 20mm which corresponds to a frequency range of roughly between 1kHz and 5kHz. To be more precise, we compute the empirical

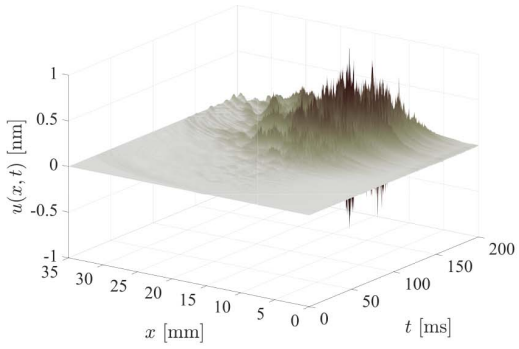

(a) Spatio-Temporal Stochastic Evolution of the BM

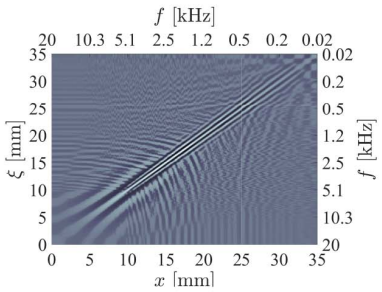

(b) Empirical Covariance $\mathbf{U}_{\text{Emp}}(x,\xi)$

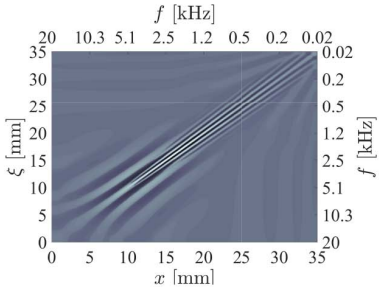

(c) Predicted Worst-Case Covariance $\mathbf{U}(x,\xi)$

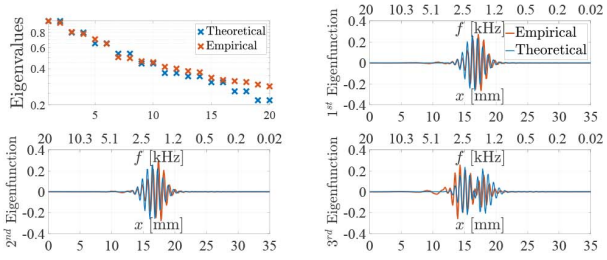

(d) Empirical and Theoretical Dominant Eigenvalues/functions

Fig. 7. Nonlinear Stochastic Simulation. Figure (a) shows the BM response to spatially uncorrelated stochastic active gain (scenario $\mathbf{S}_1$) with an expectation given by (23) where $\beta = 2$ and a perturbation of $\epsilon = 1.1 \times 10^{-5}$. Figures (b) and (c) show a comparison between the empirical and predicted covariances. The predicted covariance is computed for the linearized dynamics via the power iteration method applied on the loop gain operator (16). The empirical covariance is computed using the data obtained from one nonlinear stochastic simulation using (26) and integrated in time using (27) assuming ergodicity. Figure (d) shows a comparison between the dominant eigenvalues/functions of the empirical and predicted covariances shown in Figures (b) and (c), respectively. This eigen-decomposition is referred to as the *Karhunen-Loève* decomposition. Clearly the theoretical predictions match the empirical data, thus suggesting that the nonlinearities only saturate the response without significantly deforming the waveforms.

covariance $\mathbf{U}_{\mathrm{Emp}}(x,\xi)$ as follows

$$\mathbf{U}_{\mathrm{Emp}}(x,\xi) = \frac{1}{t_f}\int_0^{t_f} u(x,\tau)u(\xi,\tau)d\tau. \tag{27}$$

The time averaging replaces the expectation assuming ergodicity. Figures 7(b) and (c) compare the empirical covariance to the predicted worst-case covariance. By visual inspection, we observe that the empirical results are in good agreement with our theoretical predictions. For a more precise comparison, we plot the first twenty dominant eigenvalues and first three dominant eigenfunctions of both the predicted and empirical covariances in Figure 7(d). This eigen-decomposition is referred to as the *Karhunen-Loève decomposition*. The eigenfunctions are the modes of BM vibrations that have the highest growth rate and are more likely to destabilize for small perturbations of the active gain. The plots does not show any significant difference between the empirical and theoretical results. In fact, although the nonlinear active gain slightly deforms the response, but its fundamental role (in the absence of a stimulus) is to saturate the linearized instabilities to form oscillations that remain bounded in time.

VI. Discussion

The mechanisms underlying cochlear instabilities such as SOAEs and tinnitus are still controversial and not well understood. This paper suggests a new possible source of cochlear instabilities: spatio-temporal stochastic perturbations of the active gain.

It is widely accepted that Outer Hair Cells (OHC) are responsible for the active gain in the cochlea. This work proposes a *simulation-free*, system theoretic framework to analyze the effects of small stochastic perturbations that may occur at the level of the OHCs. These perturbations can have several physical origins such as noisy nearby neuronal activities, cellular activities, blood flow, etc$\cdots$ The simulation-free approach has the advantage of obtaining a more numerically efficient computation as compared to the computationally-expensive stochastic simulation.

Studying the effects of randomness in the active gain is not new [1], [2]. However, the previous studies on this matter considered random spatial perturbations that are time-invariant. This type of randomness is referred to as "frozen" or *quenched disorder* in the statistical physics community. In fact, [2] investigated the effects of the frozen spatial randomness by carrying out Monte Carlo simulations to study the statistics of the instabilities. However, to achieve a broad spectrum of unstable frequencies, the authors allowed severe perturbations of the active gain which is not realistic. Without these severe perturbations, the unstable frequencies would be limited to a band of high frequencies only (Section IV-B). This does not agree with the experimental observations where, for example, SOAEs are mainly found between 0.5 and 4.5kHz.

A more realistic case is to treat the active gain as a stochastic process, where the randomness may occur in space and time, simultaneously. In addition to that, only small perturbations of the active gain are considered (three to four orders of magnitude less than [2]). A major advantage of our analysis is that it is *simulation-free* and no Monte Carlo simulations are required to study the statistics of the emerging instabilities. In our analysis, we also show that the band of unstable frequencies can be controlled by the tuning of the structural parameters of the cochlea such as the active gain coefficient. Hence, we show that even for very small perturbations, the unstable frequencies can be shifted dramatically. Furthermore, examining localized stochastic perturbations in the active gain allowed us to observe local instabilities that shift toward the stapes as the localization length or spread is larger. This observation resembles the detuning phenomenon present in the cochlea.

VII. Conclusion and Future Work

This paper examines the instabilities that occur in the linearized dynamics due to spatio-temporal stochastic perturbations in the distributed structure of the cochlear partition. The simulation-free analysis is carried out through a structured stochastic uncertainty framework. It is shown that the spatial shape of the expectation and covariance of the gain coefficient affect the locations of the instabilities on the basilar membrane. These instabilities eventually saturate to form bounded oscillations due to the saturation nonlinearity of the active gain (3) producing spontaneous basilar membrane vibrations. It is believed that these instabilities are reflected to the middle ear as spontaneous otoacoustic emissions (SOAEs) [23] with frequencies corresponding to the location of the instability on the basilar membrane. This analysis also suggests an explanation of one possible source of tinnitus, which is less addressed in the literature. Particularly, if the spontaneous BM vibrations were intense enough, they may be perceived as tinnitus. Future work will address instabilities that may occur due to stochastic uncertainties in structural parameters other than the active gain coefficient (e.g., the cochlear fluid density).

Appendix A
Mass Operators

The fluids block in Figure 1(a) can be modeled in 1D, 2D, or 3D. In two dimensions, Navier-Stokes equations boil down to the Laplace equation with the appropriate boundary conditions as shown in [8]. This simplification is valid under the assumptions of incompressible, inviscid fluid where the magnitude of the vibrations of the membranes are negligible relative to the dimensions of the cochlea. These assumptions make the fluid block in Figure 1 memoryless and amenable to be represented by the two linear spatial operators $\mathcal{M}_f$ and $\mathcal{M}_s$ in (1). In this paper, we give these operators for the 1D case only. Higher dimensions can be treated similarly. As in [14], the fluid block in 1D can be represented by the traveling wave equation as follows

$$\frac{\partial^2}{\partial x^2}p(x,t) = \frac{2\rho}{H}\ddot{u}(x,t);\ \begin{cases} \frac{\partial}{\partial x}p(0,t) = 2\rho\ddot{s}(t) \\ p(L,t) = 0, \end{cases} \tag{28}$$

where ρ is the density of the fluid, H is the height of the fluid chamber and L is the length of the BM. This is a linear system with two inputs: $\ddot{u}$ and $\ddot{s}$. It can be shown that the solution of (28) is

$$p(x,t) = -\big[\mathcal{M}_f\ddot{u}\big](x,t) - [\mathcal{M}_s]\ddot{s}(t)$$

$$(x,t) \coloneqq -\frac{2\rho}{H}\sum_{n=0}^{\infty}\frac{1}{\lambda_n}\phi_n(x)\langle\phi_n,\ddot{u}(.,t)\rangle$$
$$(t) \coloneqq 2\rho(L-x)\ddot{s}(t), \tag{29}$$

where $\langle,\rangle$ denotes the inner product in the space of square integrable functions over [0, L], and

$$\lambda_n = -\left(n+\frac{1}{2}\right)^2\frac{\pi^2}{L^2} \longleftrightarrow \phi_n(x) = \sqrt{\frac{2}{L}}\cos\left[\left(n+\frac{1}{2}\right)\frac{\pi}{L}x\right],$$

for $n = 0, 1, 2, \ldots$ It is fairly straightforward to verify that (29) is indeed a solution by substituting in (28).

Finite dimensional approximations can be obtained by representing $\mathcal{M}_f$ and $\mathcal{M}_s$ by the matrix $M_f \in \mathbb{R}^{(N_x+1)\times(N_x+1)}$ and the vector $M_s \in \mathbb{R}^{N_x+1}$, respectively, where N_x+1 is the spatial grid size that discretizes the spatial variable x. This is done by truncating the sum and by using a quadrature rule to compute the inner product (or simply a trapezoidal rule). Note that finite difference methods, in the spirit of [14] and [12], can also be used to approximate the mass operators. However, the spectral method we presented here provides a better and more efficient approximation.

Appendix B
Matrix Approximation of Spatial Operators

Let the matrices

$$F_\eta \in \mathbb{R}^{(N_x+1)\times(N_x+1)};\quad A_0 \in \mathbb{R}^{4(N_x+1)\times 4(N_x+1)};$$
$$B_0 \in \mathbb{R}^{4(N_x+1)\times(N_x+1)};\quad \tilde{B}_0(u_n) \in \mathbb{R}^{4(N_x+1)\times(N_x+1)};$$
$$C_0 \in \mathbb{R}^{(N_x+1)\times 4(N_x+1)};\quad E \in \mathbb{R}^{4(N_x+1)\times 4(N_x+1)};$$
$$A_{\bar{\gamma}}(u_n) \in \mathbb{R}^{4(N_x+1)\times 4(N_x+1)},$$

be the finite dimensional approximations of the spatial operators $\Phi_\eta, \mathcal{A}_0, \mathcal{B}_0, \tilde{\mathcal{B}}_0(u), \mathcal{C}_0, \mathcal{E}$ and $\mathcal{A}_{\bar{\gamma}}(u_n)$, respectively. Using the trapezoidal integration rule on (4), we can construct the matrix F_η as

$$F_\eta = \mathcal{D}\Big(\tilde{F}_\eta\, T\mathbf{1}\Big)^{-1}\tilde{F}_\eta\, T,$$

where $\mathcal{D}$ is the diagonal operator, $\tilde{F}_\eta \in \mathbb{R}^{(N_x+1)\times(N_x+1)}$ and its $(i,j)^{th}$ entry is defined as $(\tilde{F}_\eta)_{ij} \coloneqq e^{-(i-j)^2\frac{\Delta_x^2}{\eta^2}}$, $\mathbf{1} \in \mathbb{R}^{N_x+1}$ is a vector whose entries are all ones and $T \in \mathbb{R}^{(N_x+1)\times(N_x+1)}$ is a diagonal matrix defined as

$$T \coloneqq \mathcal{D}\big(\big[\tfrac{1}{2} \quad 1 \quad \cdots \quad 1 \quad \tfrac{1}{2}\big]\big).$$

Furthermore, define the following diagonal matrices $\in \mathbb{R}^{(N_x+1)\times(N_x+1)}$

$$K_l \coloneqq \mathcal{D}\big(\big[k_l(x_0) \quad \cdots \quad k_l(x_{N_x})\big]\big),\quad l = 1,2,3,4;$$
$$C_l \coloneqq \mathcal{D}\big(\big[c_l(x_0) \quad \cdots \quad c_l(x_{N_x})\big]\big),\quad l = 1,2,3,4;$$
$$D_{\bar{\gamma}} \coloneqq \mathcal{D}\big(\big[\bar{\gamma}(x_0) \quad \cdots \quad \bar{\gamma}(x_{N_x})\big]\big);$$
$$\tilde{G}(u_n) \coloneqq \mathcal{D}\left(1+\frac{\theta}{R^2}F_\eta(u_n\circ u_n)\right)^{-1},$$

where $\circ$ is the Hadamard (element-by-element) product. Therefore

$$E \coloneqq \begin{bmatrix} I & 0 & 0 & 0\\ 0 & I & 0 & 0\\ 0 & 0 & \frac{g}{b}m_1 I + M_f & 0\\ 0 & 0 & 0 & m_2 I\end{bmatrix};\quad B \coloneqq \begin{bmatrix} 0\\ 0\\ -M_s\\ 0\end{bmatrix};$$

$$A_0 \coloneqq \begin{bmatrix} 0 & 0 & I & 0\\ 0 & 0 & 0 & I\\ -\frac{g}{b}(K_1+K_3) & K_3 & -\frac{g}{b}(C_1+C_3) & C_3\\ \frac{g}{b}K_3 & -(K_2+K_3) & \frac{g}{b}C_3 & -(C_2+C_3)\end{bmatrix};$$

$$B_0 \coloneqq \begin{bmatrix}0 & 0 & I & 0\end{bmatrix}^T;\quad C_0 \coloneqq \begin{bmatrix}\frac{g}{b}K_4 & -K_4 & \frac{g}{b}C_4 & -C_4\end{bmatrix};$$

$$\tilde{B}_0(u_n) \coloneqq \begin{bmatrix}0 & 0 & \tilde{G}(u_n) & 0\end{bmatrix}^T;$$

$$A_{\bar{\gamma}}(u_n) \coloneqq A_0 + \tilde{B}_0(u_n)D_{\bar{\gamma}}C_0.$$

Appendix C
System Linearization

The only nonlinear portion of the dynamics appears in the active gain given by (3). Thus, to linearize the dynamics around the origin, it suffices to linearize the active gain. Up to first order, the active gain can be expanded around some $\bar{u}$, by letting $u \coloneqq \bar{u} + \epsilon\tilde{u}$. The expansion is given by

$$\mathcal{G}(u) = \mathcal{G}(\bar{u}) + \epsilon\left[\frac{\partial}{\partial u}\mathcal{G}(\bar{u})\right](\tilde{u}) + \mathcal{O}\Big(\epsilon^2\Big),$$

where $[\frac{\partial}{\partial u}\mathcal{G}(\bar{u})](\tilde{u})$ is the directional derivative in the direction of $\tilde{u}$. It can be calculated as follows

$$\left[\frac{\partial}{\partial u}\mathcal{G}(\bar{u})\right](\tilde{u}) \coloneqq \lim_{\epsilon\to 0}\frac{\mathcal{G}(\bar{u}+\epsilon\tilde{u})-\mathcal{G}(\bar{u})}{\epsilon}$$
$$= -\frac{2\theta}{R^2}\frac{\gamma\Phi_\eta(\bar{u}\tilde{u})}{\left(1+\theta\Phi_\eta\left(\frac{u^2}{R^2}\right)\right)^2}.$$

To linearize around the origin, we set $\bar{u} = 0$. This yields

$$\mathcal{G}(0) = \gamma \qquad \text{and} \qquad \left[\frac{\partial}{\partial u}\mathcal{G}(0)\right](\tilde{u}) = 0.$$

Hence, up to first order, the linearization around the fixed point of the active gain is $\mathcal{G}(u) = \gamma + \mathcal{O}(\epsilon^2)$, which is independent of the micro-mechanical, spatial-averaging operator Φ_η.

Appendix D
Equivalent Rectangular Bandwidth

The width, η, of the Gaussian kernel in (5) controls the spatial coupling length along the BM. The numerical value of η in this paper is chosen based on the critical bands in the cochlea. In psychoacoustics, the concept of critical bands was introduced by Harvey Fletcher in 1933. He described the bands of audio frequencies within which two tones interfere in the perception of each other, thus indicating the length of spatial coupling along the cochlea. This band, which is termed Equivalent Rectangular Bandwidth (ERB), is believed to be equivalent to 0.89mm on the BM [26].

We model the spatial coupling along the BM using a Gaussian kernel as shown in (3)-(5). Hence, we require to calculate the width η of the Gaussian kernel that fits an ERB of 0.89mm as shown in Figure 8. It is fairly straight forward

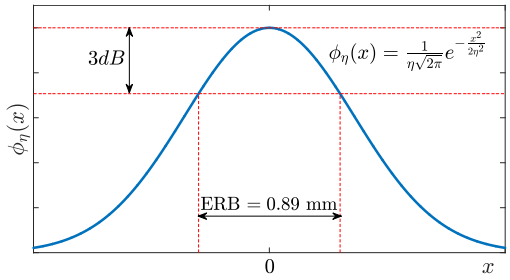

Fig. 8. Equivalent Rectangular Bandwidth (ERB). The spatial coupling in the micro-mechanical stage is modeled using a Gaussian kernel whose width is chosen to respect the ERB in the cochlea.

to calculate η, by setting $\phi_\eta(0.89/2) = \frac{\sqrt{2}}{2}\phi_\eta(0)$, we get $\eta = 0.5345$mm.

REFERENCES

[1] F. Fruth, F. Jülicher, and B. Lindner, "An active oscillator model describes the statistics of spontaneous otoacoustic emissions," *Biophys. J.*, vol. 107, no. 4, pp. 815–824, 2014.

[2] E. M. Ku, S. J. Elliott, and B. Lineton, "Statistics of instabilities in a state space model of the human cochlea," *J. Acoust. Soc. Amer.*, vol. 124, no. 2, pp. 1068–1079, 2008.

[3] M. Filo and B. Bamieh, "An input-output approach to structured stochastic uncertainty," *IEEE Trans. Autom. Control*, early access, Jan. 30, 2020, doi: 10.1109/TAC.2020.2970393.

[4] M. Filo and B. Bamieh, "An input-output approach to structured stochastic uncertainty in continuous time," 2018. [Online]. Available: arXiv:1806.09091.

[5] J. Lu and R. E. Skelton, "Mean-square small gain theorem for stochastic control: Discrete-time case," *IEEE Trans. Autom. Control*, vol. 47, no. 3, pp. 490–494, Mar. 2002.

[6] M. Filo and B. Bamieh, "Investigating cochlear instabilities using structured stochastic uncertainty," in *Proc. IEEE 56th Annu. Conf. Decis. Control (CDC)*, Melbourne, VIC, Australia, 2017, pp. 1634–1640.

[7] C. D. Geisler and C. Sang, "A cochlear model using feed-forward outer-hair-cell forces," *Hear. Res.*, vol. 86, nos. 1–2, pp. 132–146, 1995.

[8] M. D. LaMar, J. Xin, and Y. Qi, "Signal processing of acoustic signals in the time domain with an active nonlinear nonlocal cochlear model," *Signal Process.*, vol. 86, no. 2, pp. 360–374, 2006.

[9] S. T. Neely and D. Kim, "A model for active elements in cochlear biomechanics," *J. Acoust. Soc. Amer.*, vol. 79, no. 5, pp. 1472–1480, 1986.

[10] C. R. Steele and L. A. Taber, "Comparison of WKB and finite difference calculations for a two-dimensional cochlear model," *J. Acoust. Soc. Amer.*, vol. 65, no. 4, pp. 1001–1006, 1979.

[11] E. Givelberg and J. Bunn, "A comprehensive three-dimensional model of the cochlea," *J. Comput. Phys.*, vol. 191, no. 2, pp. 377–391, 2003.

[12] S. T. Neely, "Finite difference solution of a two-dimensional mathematical model of the cochlea," *J. Acoust. Soc. Amer.*, vol. 69, no. 5, pp. 1386–1393, 1981.

[13] S. J. Elliott, G. Ni, B. R. Mace, and B. Lineton, "A wave finite element analysis of the passive cochlea," *J. Acoust. Soc. Amer.*, vol. 133, no. 3, pp. 1535–1545, 2013.

[14] S. J. Elliott, E. M. Ku, and B. Lineton, "A state space model for cochlear mechanics," *J. Acoust. Soc. Amer.*, vol. 122, no. 5, pp. 2759–2771, 2007.

[15] D. Bertaccini and R. Sisto, "Fast numerical solution of nonlinear nonlocal cochlear models," *J. Comput. Phys.*, vol. 230, no. 7, pp. 2575–2587, 2011.

[16] M. Filo, F. Karameh, and M. Awad, "Order reduction and efficient implementation of nonlinear nonlocal cochlear response models," *Biol. Cybern.*, vol. 110, no. 6, pp. 435–454, 2016.

[17] M. G. Filo, "Topics in modeling of cochlear dynamics: Computation, response and stability analysis," Ph.D. dissertation, Dept. Mech. Eng. Univ. California, Santa Barbara, CA, USA, 2017.

[18] J. Meaud and K. Grosh, "The effect of tectorial membrane and basilar membrane longitudinal coupling in cochlear mechanics," *J. Acoust. Soc. Amer.*, vol. 127, no. 3, pp. 1411–1421, 2010.

[19] K. Zhou, J. C. Doyle, and K. Glover, *Robust and Optimal Control*, vol. 40. Upper Saddle River, NJ, USA: Prentice-Hall, 1996.

[20] B. Øksendal, "Stochastic differential equations," in *Stochastic Differential Equations*. Heidelberg, Germany: Springer, 2003, pp. 65–84.

[21] P. A. Parrilo and S. Khatri, "On cone-invariant linear matrix inequalities," *IEEE Trans. Autom. Control*, vol. 45, no. 8, pp. 1558–1563, Aug. 2000.

[22] D. D. Greenwood, "A cochlear frequency-position function for several species–29 years later," *J. Acoust. Soc. Amer.*, vol. 87, no. 6, pp. 2592–2605, 1990.

[23] A. Nuttall, K. Grosh, J. Zheng, E. De Boer, Y. Zou, and T. Ren, "Spontaneous basilar membrane oscillation and otoacoustic emission at 15 KHz in a Guinea pig," *J. Assoc. Res. Otolaryngol.*, vol. 5, no. 4, pp. 337–348, 2004.

[24] M. Penner, "An estimate of the prevalence of tinnitus caused by spontaneous otoacoustic emissions," *Archives Otolaryngol. Head Neck Surg.*, vol. 116, no. 4, pp. 418–423, 1990.

[25] G. Maruyama, "Continuous Markov processes and stochastic equations," *Rendiconti del Circolo Matematico di Palermo*, vol. 4, no. 1, p. 48, 1955.

[26] B. Moore, "Parallels between frequency selectivity measured psychophysically and in cochlear mechanics," *Scandinavian Audiol. Suppl.* vol. 25, pp. 139–152, Jan. 1986.

Maurice Filo (Member, IEEE) received the Dipl.Ing. degree from Lebanese University in 2010, the M.Sc. degree in electrical engineering from the American University of Beirut in 2013, and the M.Sc. and Ph.D. degrees in mechanical engineering from the University of California at Santa Barbara in 2017 and 2018, respectively. He was a Postdoctoral Researcher with the Swiss Federal Institute of Technology, ETH Zürich. His research interests include stochastic biomolecular dynamics, distributed dynamical systems, cochlear dynamics, mobile sensing, and optimal control and estimation. He was a recipient of the 2019 CCDC Best Ph.D. Thesis Award, the 2013 CCDC Outstanding Scholar Fellowship, and the Institute for Energy Efficiency Holbrook Foundation Fellowship.

Bassam Bamieh (Fellow, IEEE) received the B.Sc. degree in electrical engineering and physics from Valparaiso University, Valparaiso, IN, USA, in 1983, and the M.Sc. and Ph.D. degrees in electrical and computer engineering from Rice University, Houston, TX, USA, in 1986 and 1992, respectively. From 1991 to 1998, he was an Assistant Professor with the Department of Electrical and Computer Engineering, and the Coordinated Science Laboratory, University of Illinois at Urbana–Champaign. He joined the University of California at Santa Barbara, where he is currently a Professor of mechanical engineering. His research interests include robust and optimal control, distributed and networked control and dynamical systems, shear flow transition and turbulence, and the use of feedback in thermoacoustic energy conversion devices. He was a recipient of the IEEE Control Systems Society G. S. Axelby Outstanding Paper Award (twice), the AACC Hugo Schuck Best Paper Award, and the National Science Foundation CAREER Award. He was elected as a Distinguished Lecturer of the IEEE Control Systems Society in 2005, and a Fellow of the International Federation of Automatic Control.